nature physics

ARTICLES

https://doi.org/10.1038/s41567-020-0936-3

Check for updates

Polarizing an antiferromagnet by optical engineering of the crystal field

Ankit S. Disa[1,2] ✉, Michael Fechner[1], Tobia F. Nova[1], Biaolong Liu[1], Michael Först[1], Dharmalingam Prabhakaran[3], Paolo G. Radaelli[3] and Andrea Cavalleri[1,2,3] ✉

Strain engineering is widely used to manipulate the electronic and magnetic properties of complex materials. For example, the piezomagnetic effect provides an attractive route to control magnetism with strain. In this effect, the staggered spin structure of an antiferromagnet is decompensated by breaking the crystal field symmetry, which induces a ferrimagnetic polarization. Piezomagnetism is especially appealing because, unlike magnetostriction, it couples strain and magnetization at linear order, and allows for bi-directional control suitable for memory and spintronics applications. However, its use in functional devices has so far been hindered by the slow speed and large uniaxial strains required. Here we show that the essential features of piezomagnetism can be reproduced with optical phonons alone, which can be driven by light to large amplitudes without changing the volume and hence beyond the elastic limits of the material. We exploit nonlinear, three-phonon mixing to induce the desired crystal field distortions in the antiferromagnet CoF_2. Through this effect, we generate a ferrimagnetic moment of 0.2 μ_B per unit cell, nearly three orders of magnitude larger than achieved with mechanical strain.

The control of magnetism via strain is most commonly based on magnetostriction. This effect relates an induced magnetization to the square of the applied stress and is restricted to systems with an equilibrium magnetization, like ferromagnets. Because the coupling is quadratic, the magnetic moment is only modulated in one direction when no external field is present.

Piezomagnetism, on the other hand, is a property of certain antiferromagnetic materials, which manifests as a linear coupling between an applied stress σ and an induced magnetization M of the form $M_i = \Lambda_{ijk}\sigma_{jk}$, where Λ is the piezomagnetic tensor[1,2]. Hence, by exploiting the piezomagnetic effect, one can induce a magnetization of either sign from a crystal that possesses no net magnetization (see Fig. 1a).

CoF_2 is one of the simplest known piezomagnetic crystals. It has a rutile crystal structure with a body-centred cubic arrangement of cobalt ions, each surrounded by a fluorine octahedron with a tetragonal crystal field[3,4]. Below the Néel temperature $T_N = 39$ K, it is a fully compensated type I antiferromagnet with easy-axis anisotropy, such that the magnetic moments on the Co ions at the centre and corner of the cube point along the tetragonal c axis with opposite sign (magnetic space group $P4_2'/mnm'$; see Fig. 1a)[5,6]. Piezomagnetism in CoF_2 arises from the site-selective modification of the Co crystal fields[7,8]. Strain along the [110] direction distorts the crystal structure in such a way that the in-plane Co–F bond is shortened for the central sublattice and lengthened for the corner one (or vice versa). As result, the relative energy splitting Δ of the Co t_{2g} orbitals is decreased on one site and increased on the other (Fig. 1b). In the d^7 configuration, the orbital magnetic moment scales as $m_L \sim \Delta^{-1}$ (refs.[9,10]); hence, the strain-induced distortion decompensates the antiferromagnetically ordered moments and generates a net ferrimagnetic polarization. By changing the direction of the strain from tensile to compressive, the direction of the crystal field distortion reverses, and with that the sign of the induced magnetization.

The essential microscopic ingredient in the piezomagnetic effect is the antiparallel distortion of the Co–F bonds on each sublattice. Hence, it could also be induced through the displacements of certain optical phonons alone, with the advantage that such displacements preserve the cell volume. New optical devices enabling resonant driving of lattice vibrations at mid-infrared and terahertz (THz) frequencies open up the possibility of selectively controlling the structure of solids with light[11–14]. At large phonon amplitudes, lattice nonlinearities can be exploited to rectify atomic displacements and coherently mimic the effect of heteroepitaxial or externally applied strain[15,16]. In particular, it was recently suggested that a rectification of the B_{2g} Raman phonon in CoF_2 would produce the same relative bond displacements as [110] uniaxial strain[17], but at constant unit-cell volume.

Here, we validate this approach and generate light-induced ferrimagnetic order in CoF_2 by using the anharmonic coupling of three volume-preserving optical phonons to drive symmetry-breaking lattice distortions. In contrast to the case of applied strain, this dynamical piezomagnetic effect creates orders-of-magnitude larger displacements on timescales not limited by the speed of sound.

Lattice engineering by nonlinear phononics

The desired lattice distortion corresponds to atomic motions along the coordinates of a Raman-active phonon of B_{2g} symmetry. Hence, it cannot be directly excited by light. Moreover, a purely impulsive excitation, typically achieved using visible or near-infrared pulses, would produce an oscillating vibration about the equilibrium atomic positions and no net displacement of the lattice. Instead, we use the nonlinear coupling between resonantly driven infrared-active (IR) phonons and the Raman (R) mode, which can provide directional atomic motions away from equilibrium.

Figure 2 describes the anharmonic lattice interaction used to drive the dynamical piezomagnetic effect[13,17]. The lowest-order phonon coupling is given by the energy term $U = Q_{IR,1}Q_{IR,2}Q_R$, where Q_{IR} and Q_R denote infrared and Raman mode coordinates (subscript 1 and 2 denote different phonons). In the case that Q_R has B_{2g} symmetry, this coupling is symmetry-allowed if $Q_{IR,1}$ and $Q_{IR,2}$ both have

[1]Max Planck Institute for the Structure and Dynamics of Matter, Hamburg, Germany. [2]The Hamburg Centre for Ultrafast Imaging, Hamburg, Germany. [3]Clarendon Laboratory, Department of Physics, Oxford University, Oxford, UK. ✉e-mail: ankit.disa@mpsd.mpg.de; andrea.cavalleri@mpsd.mpg.de

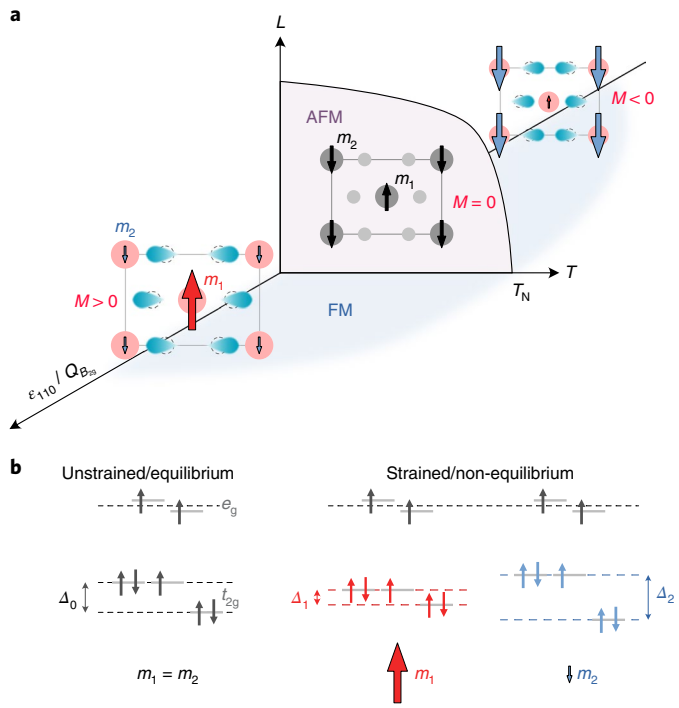

Fig. 1 | Piezomagnetic effect in CoF_2. **a**, Under no strain, CoF_2 is antiferromagnetic below T_N. By appropriate lattice deformation, the antiferromagnetically aligned moments on the Co sites (m_1 and m_2) decompensate, leading to ferrimagnetic order and non-zero magnetization (M). The lattice distortion (depicted in the a–c plane) can be created by uniaxial strain along the crystallographic [110] direction (ε_{110}) or by atomic displacements along the B_{2g} Raman phonon (Q_{B2g}). **b**, The d-electron crystal field levels for CoF_2, showing the origin of the piezomagnetic moment. The energy splitting between the t_{2g} levels (Δ) determines the orbital contribution to the magnetic moment ($m_L \sim \Delta^{-1}$). In the undistorted structure (left), Δ is the same for the two Co sites. When distorted (right), Δ shrinks for one site and grows for the other, hence changing the relative magnitudes of m_1 and m_2.

E_u symmetry. If the two modes are orthogonal and degenerate, this coupling provides a force onto Q_R that follows the envelope of the two optically driven IR modes, leading to a rectified displacement of the lattice along the B_{2g} mode direction (Fig. 2a). The time-averaged displacement of Q_R is proportional to the product of the two IR mode amplitudes, $Q_R \propto |Q_{IR,a}||Q_{IR,b}| \cos \Delta\phi_{ab}$, where $\Delta\phi_{ab}$ is the relative phase of the two modes. Hence, the lattice displacement is maximal when the two IR modes are driven in phase, and the direction of the displacement flips when one of the two IR modes changes sign (that is, $\Delta\phi_{ab} = \pi$), as shown in Fig. 2b, c. In CoF_2, the induced ferrimagnetic moment is linearly proportional to this $Q_R(B_{2g})$ displacement (see Supplementary Section 2.4).

Experimental approach

Experimentally, to create the required lattice distortion and generate a net magnetization, one must simultaneously drive two degenerate, orthogonal IR modes with E_u symmetry. Figure 3a shows the optical conductivity along the a and b axes measured on the 100-μm-thick CoF_2 crystal used in this experiment. The three conductivity peaks identify different E_u phonons with resonant frequencies close to 6, 8 and 12 THz. We resonantly and simultaneously drove the two IR modes at 12 THz (atomic motions also shown in Fig. 3a), for which the largest anharmonic coupling to the B_{2g} Raman mode was predicted (see Supplementary Table 3).

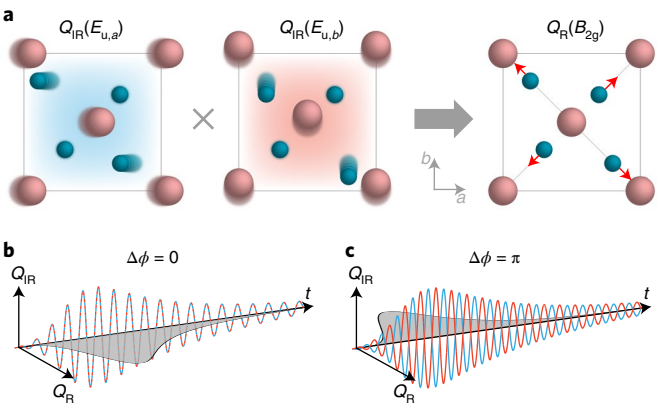

Fig. 2 | Breaking symmetry with phonons. **a**, Two orthogonal, degenerate E_u phonons mix nonlinearly to displace the lattice along the B_{2g} Raman mode coordinate. The force on the lattice arising from the nonlinear interaction ($\mathbf{F}_{Q_R}$) is shown by red arrows. **b**, The dynamics of the two IR modes (in red and blue) and the Raman mode (in grey) resulting from resonant excitation of both E_u modes by a THz pulse. The IR modes oscillate about their equilibrium positions, while the Raman mode is displaced away from equilibrium, creating a time-averaged structural distortion (solid shading). The two IR modes in this case are pumped in phase ($\Delta\phi_{ab} = 0$). **c**, The phonon dynamics for the case when one of the two IR modes is driven with opposite sign ($\Delta\phi_{ab} = \pi$), showing that the Raman mode is displaced in the opposite direction. Note that in both cases, the motions of the atoms are linear.

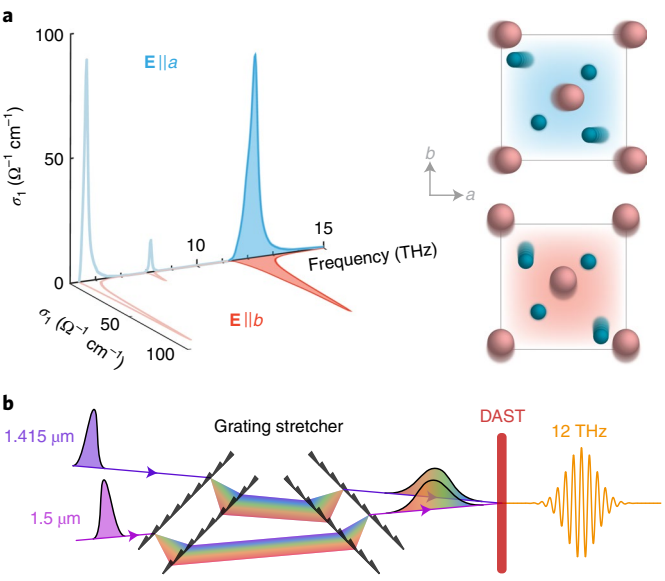

Fig. 3 | Driving degenerate infrared phonons in CoF_2. **a**, Left, optical conductivity of CoF_2 at 6 K along the two orthogonal in-plane crystal axes (a and b in blue and red, respectively). The three peaks arise from the doubly degenerate (E_u symmetry) IR phonons. We pump the modes at 12 THz (solid shading). Right, a top view of the atomic motions of the two pumped modes. **b**, Depiction of the chirped-pulse DFG process for the pump pulses used in this experiment. Two near-IR pulses generated from co-seeded optical parametric amplifiers are stretched using two transmission grating pairs and combined non-collinearly on the organic crystal DAST (4-*N*,*N*-dimethylamino-4′-*N*′-methyl-stilbazolium tosylate) to produce narrow-bandwidth, high-intensity pulses with a centre frequency of 12 THz.

Intense THz excitation pulses were generated in a specially designed optical device that is based on two optical parametric amplifiers, a chirping stage, and a difference frequency generation

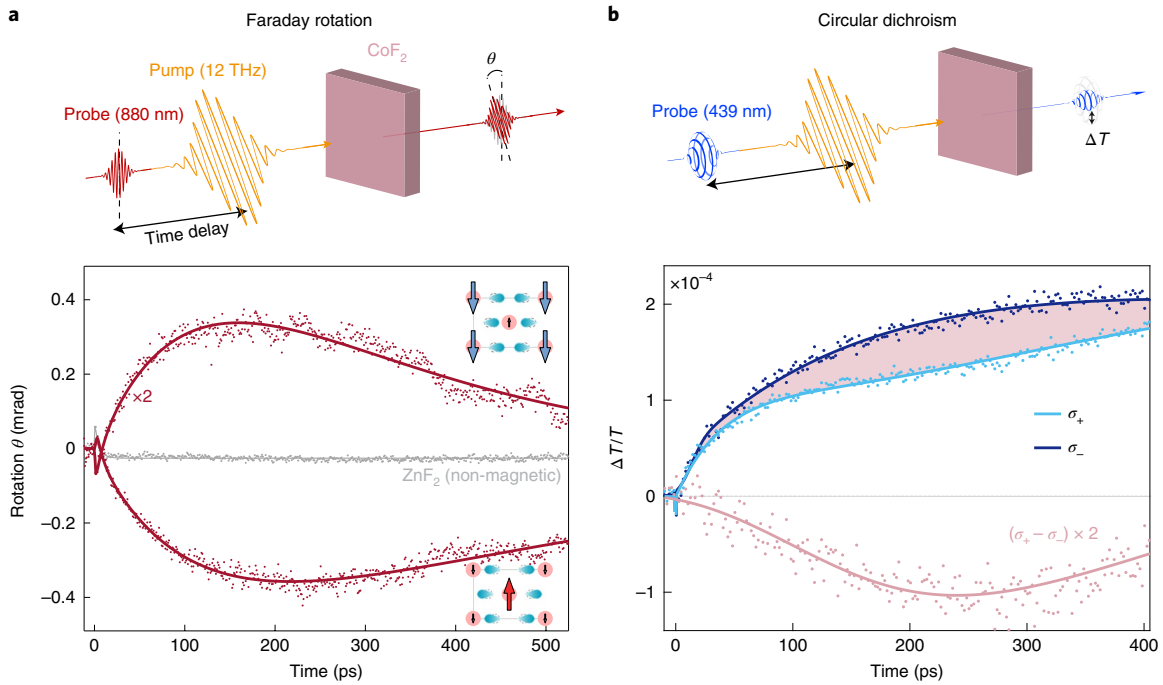

Fig. 4 | Time-resolved magneto-optical measurements. a, Top, depiction of the measurement set-up with THz pump and Faraday rotation probe. The 12-THz pump pulse was oriented at 45° with respect to the crystallographic *a* and *b* axes, and the polarization rotation angle of a subsequent 880-nm probe pulse was detected. Bottom, Faraday rotation data on CoF_2 (red) for two polarizations of the pump pulse (+45° and −45°) as a function of time delay. They display similar time dependences, with a small signal at short times that reverses, saturates and eventually decays back to zero. The inset shows the induced structural distortion (in the *a*–*c* plane) and resulting ferrimagnetic state for the two pump polarizations. The same measurement taken on ZnF_2 is plotted in grey, exhibiting no long-lived response. **b**, Top, depiction of the measurement set-up with THz pump and circular dichroism probe (top). The absorption of left and right circularly polarized probe pulses at 439 nm is detected as a function of time delay. Bottom, the relative change in transmission for left (dark blue) and right (light blue) circularly polarized probe pulses. The shaded area depicts the circular dichroism, which is plotted on a ×2 scale in pink. The time dependence of the circular dichroism matches that of the Faraday rotation. In all panels, dots are measured data points and solid lines are fits (see Methods).

(DFG) stage that uses an organic crystal[18], as depicted in Fig. 3b. We produced 500-fs-long pulses with peak electric fields up to about 10 MV cm^{-1} and a centre frequency of 12 THz (see Methods). To excite both *a*- and *b*-axis modes simultaneously, the linearly polarized pump pulses were oriented at 45° with respect to the crystallographic axes (that is, oriented along the [110] direction), impinging normally to the (001) face of the crystal. The sign of the induced Q_R displacement could then be flipped by rotating the pump polarization by 90° (along [1$\bar{1}$0]). The induced magnetization was detected by complementary Faraday rotation and circular dichroism measurements at near-IR/visible wavelengths.

Optically driven magnetic phase control

Time-resolved Faraday rotation measurements taken at $T = 4$ K are shown in Fig. 4a. Without the pump, no detectable rotation was observed. After photo-excitation, a pump-induced magnetization signal developed, which switched sign after 7 ps and continued to grow in magnitude before reaching a maximum after roughly 200 ps. Rotating the pump polarization by 90° reversed the sign of the Faraday rotation, as expected from the anharmonic coupling mechanism discussed above. As a comparison, we conducted the same experiment on a ZnF_2 crystal, which has a nearly identical phonon spectrum to CoF_2, but is non-magnetic[19,20]. The ZnF_2 crystal showed only a prompt polarization rotation (arising from pump-induced birefringence) and no long-lived signal, suggesting that the signal observed in CoF_2 is of magnetic origin.

To confirm the magnetic nature of the signal, we also carried out time-resolved circular dichroism measurements (Fig. 4b). At equilibrium, circular dichroism has been observed in CoF_2 near magnetically active electronic transitions in the presence of a large externally applied magnetic field, with the strongest effect found at the 439-nm absorption line[21,22]. We probed the pump-induced change in transmission ($\Delta T/T$) at this wavelength using left and right circularly polarized pulses. A large difference in the relative $\Delta T/T$ was detected for the two polarizations after the THz pump excitation, with a timescale matching that of the Faraday rotation measurements.

Taken together, the observations reported above are evidence of a non-equilibrium state with a net magnetization and a response time of approximately 100 ps.

Characterization of induced ferrimagnetic state

Figure 5a shows the magnitude of the pump-induced Faraday rotation and circular dichroism as a function of temperature. Both signals reduced upon warming the sample from 4 K and vanished above 40 K, coinciding with T_N. The temperature evolution of the non-equilibrium magnetization followed that of the static piezomagnetic response of CoF_2 (ref. [23]). In both cases, the magnitude of the induced ferrimagnetic polarization should scale with the staggered magnetization of the equilibrium antiferromagnetic state.

The dependence of the Faraday rotation signal on the peak electric field of the pump pulse is shown in Fig. 5b. Using the Verdet constant for CoF_2 (ref. [24]), we determined the induced magnetic moment at the sample surface m_{ind} and found that it scales as the square of the pump electric field (see Methods). Since the electric field linearly excites the two IR modes along the *a* and *b* axes ($Q_{IR,a}$ and $Q_{IR,b}$) and we expect $m_{ind} \propto Q_R$, this quadratic field dependence is consistent with the three-phonon coupling ($Q_{IR,a}Q_{IR,b}Q_R$)

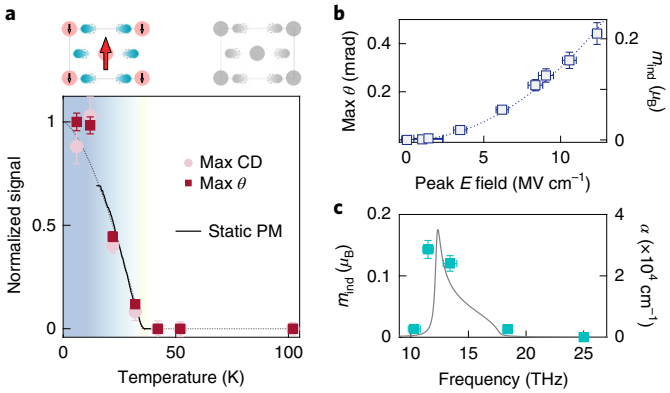

Fig. 5 | Characterization of the pump-induced state. a, Temperature dependence of the maximum of the pump-induced Faraday rotation angle (θ) and circular dichroism (CD) normalized to their values at 4 K (see Methods). The static piezomagnetic (PM) response is shown in solid black (adapted from ref. [23]), and the dotted line is a guide to the eye. The insets at the top show the dynamical piezomagnetic state in the a–c plane below T_N, and the distorted (but not magnetically ordered) state above T_N. **b**, Dependence of the maximum θ, and the associated induced magnetic moment per unit cell (m_{ind}), on the pump peak electric field. **c**, Pump frequency dependence of m_{ind} for a peak field of 10 MV cm^{-1} (solid squares, left axis) and extinction coefficient α of the phonon (solid grey, right axis). The vertical error bars were derived from the 1σ confidence interval of the fit to the time dependence of θ. The horizontal error bars in **b** and **c** denote the systematic uncertainty of the THz power calibration and the FWHM of the pump spectrum, respectively. See Methods for more details.

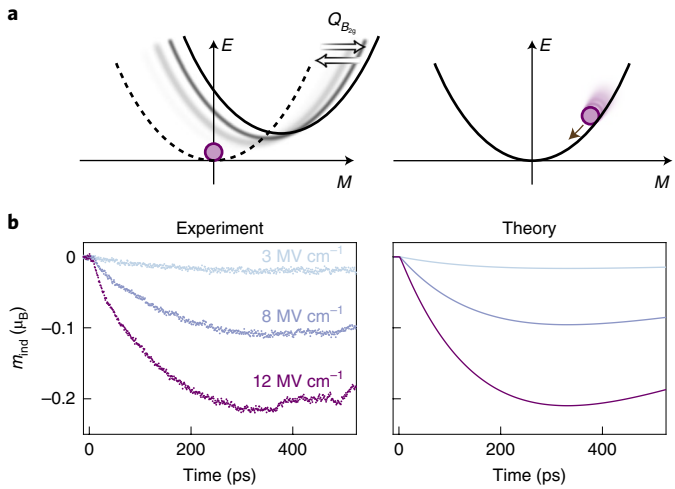

Fig. 6 | Pump-induced magnetization dynamics. a, Left, illustration of the shift of the free-energy minimum to non-zero magnetization (M) and back upon displacing $Q_{B_{2g}}$; and right, the subsequent evolution of the system in the equilibrium energy landscape. **b**, Comparison between experiment and theory for the time dependence of the induced magnetic moment per unit cell for different pump electric field strengths. The theoretical calculations are obtained from the model described in the text and depicted in **a**; the early time response, given by the non-magnetic pump-induced birefringence, has been subtracted from the experimental data (see Methods and Supplementary Section 3.2).

described in Fig. 3. Moreover, as a function of pump wavelength, the magnitude of the non-equilibrium moment showed a resonant enhancement at the eigenfrequency of the E_u phonon, as shown in Fig. 5c, demonstrating that the magnetization dynamics are indeed driven by the excited optical phonons.

We also found that at the maximum pump electric field of 12 MV cm^{-1}, the induced magnetic moment reached $m_{ind} \approx 0.2\ \mu_B$ per unit cell, in agreement with predictions from first-principles calculations (Supplementary Fig. 4). This value is more than 400 times greater than the largest reported piezomagnetic moment induced statically in CoF_2 (ref. [7]). From the known piezomagnetic coefficients, a uniaxial stress of 40 GPa would be required to generate an equivalent moment, whereas typical tensile strengths of fluoride and oxide single crystals are smaller than 0.5 GPa (ref. [25]). Since our pump excitation selectively distorted the $Q_{B_{2g}}$ mode without deforming the unit cell, much larger atomic displacements could be imposed than are possible with static strain (up to 2% of the equilibrium bond length for the experimental pump fields; see Supplementary Section 2). We estimate that, with stronger pump field strengths, an induced magnetic moment up to approximately 0.45 μ_B per unit cell could be achieved before breakdown of the CoF_2 crystal.

Discussion

We now turn to a discussion of the dynamic behaviour of the light-induced magnetization. A minimal model can be obtained from a free-energy description including the coupling between the antiferromagnetic order parameter (L), the induced magnetization (M) and the B_{2g} structural distortion (Q_R) (detailed in Supplementary Section 3). In this picture, the system initially occupies a minimum in the energy landscape where $M=0$ and $L\neq0$ (Fig. 6a). The magnetization dynamics are activated by the B_{2g} phonon displacement, which shifts the energy minimum to finite M and back on the timescale of the phonon lifetime (on the order of 5 ps). The subsequent evolution of the magnetic system after this prompt stimulus can be described as an overdamped oscillator: the kinetic energy imparted by the drive leads to the inertial growth of M, and at longer times the generated angular momentum equilibrates through spin-lattice relaxation processes[26,27]. Figure 6b shows the computed $M(t)$ from this model for different values of the driving electric field, which reproduces the experimental features well.

The proposed model provides an intuitive description of the experimentally observed magnetization dynamics. Microscopically, the dynamics of the magnetic moments of each sublattice are described by coupled Landau–Lifshitz–Bloch equations[28,29]. In this framework, the observed growth and decay may arise from the slow longitudinal relaxation of M after the impulsive drive, with a timescale associated with the equilibration of the moments on the two sublattices. An outstanding question is the transfer mechanism between the prompt g-factor imbalance (created by the phonon) and the moment imbalance observed at later times (see Supplementary Section 3.3). One possibility is that the B_{2g} mode displacement modulates the anisotropy and exchange fields, which would split the frequency of the magnons (collective magnetic excitations) and could lead to the observed time-dependent behaviour. Another possibility is that the transient lattice distortion is reinforced by the induced magnetization, creating a metastable state with slow dynamics, as has been observed in light-induced ferroelectrics[16].

The demonstrated phonon-driven, ultrafast analogue of the piezomagnetic effect provides a new mechanism to manipulate magnetism in antiferromagnetic systems[30], potentially benefiting emerging spintronics applications[31,32]. Moreover, this dynamical effect circumvents typical limits of strain control, offering possibilities to explore new out-of-equilibrium phase behaviour of correlated materials (like unconventional superconductors[33,34]) and generate light-induced functional responses under extreme lattice deformations. This approach differs from previous optical[35] and phononic[14,36] methods of magnetic phase control, as it represents the rare case of a phase transition driven by coherent light-induced breaking of lattice symmetry.

Online content

Any methods, additional references, Nature Research reporting summaries, source data, extended data, supplementary information, acknowledgements, peer review information; details of author contributions and competing interests; and statements of data and code availability are available at https://doi.org/10.1038/s41567-020-0936-3.

Received: 7 January 2020; Accepted: 11 May 2020;
Published online: 22 June 2020

References

1. Dzialoshinskii, I. E. The problem of piezomagnetism. *Sov. Phys. JETP* **6**, 621–622 (1958).
2. Borovik-Romanov, A. S. Piezomagnetism, linear magnetostriction and magnetooptic effect. *Ferroelectrics* **162**, 153–159 (1994).
3. Oelkrug, D. Absorption spectra and ligand field parameters of tetragonal 3*d*-transition metal fluorides. In *Structure and Bonding* Vol. 9, 1–26 (Springer, 1971).
4. O'Toole, N. J. & Streltsov, V. A. Synchrotron X-ray analysis of the electron density in CoF_2 and ZnF_2. *Acta Crystallogr. B* **57**, 128–135 (2001).
5. Stout, J. W. & Matarrese, L. M. Magnetic anisotropy of the iron-group fluorides. *Rev. Mod. Phys.* **25**, 338–343 (1953).
6. Erickson, R. A. Neutron diffraction studies of antiferromagnetism in manganous fluoride and some isomorphous compounds. *Phys. Rev.* **90**, 779–785 (1953).
7. Borovik-Romanov, A. S. Piezomagnetism in the antiferromagnetic fluorides of cobalt and manganese. *Sov. Phys. JETP* **11**, 786–793 (1960).
8. Moriya, T. Piezomagnetism in CoF_2. *J. Phys. Chem. Solids* **11**, 73–77 (1959).
9. Abrabam, A. & Pryce, M. H. L. The theory of paramagnetic resonance in hydrated cobalt salts. *Proc. R. Soc. Lond. A* **206**, 173–191 (1997).
10. Figgis, B. N. & Lewis, J. in *Progress in Inorganic Chemistry*, Vol. 6 (ed. Cotton, F. A.) 37–239 (Wiley, 1964).
11. von Hoegen, A., Mankowsky, R., Fechner, M., Först, M. & Cavalleri, A. Probing the interatomic potential of solids with strong-field nonlinear phononics. *Nature* **555**, 79–82 (2018).
12. Först, M. et al. Nonlinear phononics as an ultrafast route to lattice control. *Nat. Phys.* **7**, 854–856 (2011).
13. Juraschek, D. M., Fechner, M. & Spaldin, N. A. Ultrafast structure switching through nonlinear phononics. *Phys. Rev. Lett.* **118**, 054101 (2017).
14. Nova, T. F. et al. An effective magnetic field from optically driven phonons. *Nat. Phys.* **13**, 132–136 (2016).
15. Mankowsky, R. et al. Nonlinear lattice dynamics as a basis for enhanced superconductivity in $YBa_2Cu_3O_{6.5}$. *Nature* **516**, 71–73 (2014).
16. Nova, T. F., Disa, A. S., Fechner, M. & Cavalleri, A. Metastable ferroelectricity in optically strained $SrTiO_3$. *Science* **364**, 1075–1079 (2019).
17. Radaelli, P. G. Breaking symmetry with light: ultrafast ferroelectricity and magnetism from three-phonon coupling. *Phys. Rev. B* **97**, 085145 (2018).
18. Liu, B. et al. Generation of narrowband, high-intensity, carrier-envelope phase-stable pulses tunable between 4 and 18 THz. *Opt. Lett.* **42**, 129–131 (2016).
19. Balkanski, M., Moch, P. & Parisot, G. Infrared lattice-vibration spectra in NiF_2, CoF_2, and FeF_2. *J. Chem. Phys.* **44**, 940–944 (1966).
20. Giordano, J. & Benoit, C. Infrared spectra of iron, zinc and magnesium fluorides. I. Analysis of results. *J. Phys. C* **21**, 2749–2770 (1988).
21. Wong, Y. H., Scarpace, F. L., Pfeifer, C. D. & Yen, W. M. Circular and magnetic circular dichroism of some simple antiferromagnetic fluorides. *Phys. Rev. B* **9**, 3086–3096 (1974).
22. Kharchenko, N., Mil'ner, A., Eremenko, V. & Bibik, A. Magnetic circular dichroism in antiferromagnetic cobalt fluoride. *Zh. Eksp. Teor. Fiz.* **94**, 340–349 (1988).
23. Gaydamak, T. N. et al. Acoustopiezomagnetism and the elastic moduli of CoF_2. *Low. Temp. Phys.* **40**, 524–530 (2014).
24. Kharchenko, N. F. The linear magneto-optic effect as a manifestation of a higher order magnetoelectric effect. *Ferroelectrics* **162**, 173–189 (1994).
25. Bolz, R. E. *CRC Handbook of Tables for Applied Engineering Science* 2nd edn (CRC, 1973).
26. Kimel, A. V. et al. Inertia-driven spin switching in antiferromagnets. *Nat. Phys.* **5**, 727–731 (2009).
27. Maehrlein, S. F. et al. Dissecting spin-phonon equilibration in ferrimagnetic insulators by ultrafast lattice excitation. *Sci. Adv.* **4**, eaar5164 (2018).
28. Atxitia, U., Nieves, P. & Chubykalo-Fesenko, O. Landau–Lifshitz–Bloch equation for ferrimagnetic materials. *Phys. Rev. B* **86**, 104414 (2012).
29. Atxitia, U., Hinzke, D. & Nowak, U. Fundamentals and applications of the Landau–Lifshitz–Bloch equation. *J. Phys. D* **50**, 033003 (2017).
30. Song, C. et al. How to manipulate magnetic states of antiferromagnets. *Nanotechnology* **29**, 112001 (2018).
31. Baltz, V. et al. Antiferromagnetic spintronics. *Rev. Mod. Phys.* **90**, 015005 (2018).
32. Liu, Z. et al. Antiferromagnetic piezospintronics. *Adv. Electron. Mater.* **5**, 1900176 (2019).
33. Chu, J. H., Kuo, H. H., Analytis, J. G. & Fisher, I. R. Divergent nematic susceptibility in an iron arsenide superconductor. *Science* **337**, 710–712 (2012).
34. Hicks, C. W. et al. Strong increase of T_c of Sr_2RuO_4 under both tensile and compressive strain. *Science* **344**, 283–285 (2014).
35. Kirilyuk, A., Kimel, A. V. & Rasing, T. Ultrafast optical manipulation of magnetic order. *Rev. Mod. Phys.* **82**, 2731–2784 (2010).
36. Juraschek, D. M., Fechner, M., Balatsky, A. V. & Spaldin, N. A. Dynamical multiferroicity. *Phys. Rev. Mater.* **1**, 014401 (2017).

Methods

Experimental set-up. A schematic of the THz pump/optical probe set-up for this experiment is shown in Supplementary Fig. 1. We used the output of a Ti:sapphire amplifier (800 nm wavelength, 100 fs duration, 5 mJ pulse energy, 1 kHz repetition rate) to pump two optical parametric amplifiers (OPA). The signal output of each OPA had roughly 350 μJ pulse energy and 75 fs pulse duration with independently tunable centre wavelengths in the near-infrared.

The THz pump pulses were generated through a chirped DFG process, similar to ref. [18], by mixing the two OPA signal outputs in the organic crystal DAST (4-*N*,*N*-dimethylamino-4′-*N*′-methyl-stilbazolium tosylate). Before impinging on the DAST crystal, the near-infrared signal pulses were stretched by two transmission grating pairs to minimize optical rectification and produce narrow-bandwidth THz pulses. For the generation of pulses with 12 THz centre frequency by DFG, the two signal wavelengths were chosen to be 1.5 μm and 1.415 μm. For the pump frequency dependence, one signal wavelength was fixed at 1.5 μm, while the other was varied to achieve the desired difference frequency. The frequency of the resulting THz pulses was measured by a Fourier transform infrared interferometer, and their electric field profile was detected via electro-optic sampling in GaSe (Supplementary Fig. 2). The pump pulses for this experiment had durations of 400–600 fs (1 THz bandwidth) and maximum pulse energies of about 2 mJ.

The probe pulses for the Faraday rotation measurements were derived from a non-collinear OPA (NOPA) pumped by a portion of the 800 nm laser amplifier output. The NOPA provided pulses with less than 45 fs duration centred around 880 nm wavelength. After passing through the sample, the transmitted probe beam was split by a polarizing Wollaston prism into two orthogonal linear components (P and S). The two polarization components were measured by a balanced Si photodetector to determine the rotation angle.

For the magnetic circular dichroism measurements, the NOPA output was sent through a 2-mm-thick crystal of beta barium borate, phase matched to generate pulses with 439 nm centre wavelength and 2 nm bandwidth. Before impinging on the sample, the 439-nm pulses were sent through a linear polarizer and a quarter-wave plate to create circularly polarized pulses (either σ_+ or σ_-). A photomultiplier tube was used to detect the intensity of the transmitted beam after the sample, and the relative transmission of the two orthogonal components was compared to extract the circular dichroism.

Sample preparation and measurement. The CoF_2 crystals were grown using the Bridgman technique starting from ultra-dry, high-purity (>99.99%) CoF_2 powder. Growth was attempted using both a Pt–10%Rh tube and a pointed-bottom graphite crucible of 10 mm inner diameter, with the latter yielding better crystal quality. In an oxygen-free glove box, the powder was loaded into the crucible, sealed with a plug and inserted into a radio-frequency induction furnace. The crucible was first scanned at a rate of 50 mm h^{-1} to melt the powder under an argon atmosphere ($T \approx 1{,}400$ °C), and a second scan was carried out at a slower rate of 10 mm h^{-1}. The phase purity and quality of the crystal were assessed by X-ray diffraction.

For the optical experiments, a 100-μm-thick (001)-oriented CoF_2 single crystal was used. A 100-μm-thick (001)-oriented ZnF_2 crystal grown using similar methods was also used for reference experiments. The pump and probe pulses were focused on the sample surface at normal incidence. The THz pump was linearly polarized with the polarization oriented at 45° with respect to the *a* and *b* axes of the crystal (along either the [110] or [1$\bar{1}$0] crystallographic directions). For the Faraday rotation measurements, the probe polarization was orthogonal to that of the pump before the sample. At the sample position, the size of the pump spot was approximately 70 μm full-width at half-maximum (FWHM), and the probe size was roughly half that of the pump.

The measurements were carried out in a helium-flow cryostat with a base temperature of 4 K. In the antiferromagnetic phase in CoF_2, there are two possible orientations of the antiferromagnetic order parameter (180° with respect to each other). To reduce the domain distribution, we applied a small (<1 mT) magnetic field along the *c* axis while cooling below T_N (39 K), which was previously shown to stabilize large volume fractions of single 180° antiferromagnetic domains in MnF_2 (ref. [37]).

Data fitting and analysis. The pump-probe measurements (Fig. 4) were fitted by functions of the form

$$\theta(t) = A\left(\mathrm{erf}\left(\frac{t}{\sigma_1}\right)+1\right)e^{-\frac{t}{\tau_1}} + B\left(1-e^{-\frac{t}{\sigma_2}}\right)e^{-\frac{t}{\tau_2}},$$

where erf(t) is the error function. The first term represents the early time response attributed to coherent phonon dynamics ($t \leq 6$ ps), and the second term describes the long-term growth and decay as discussed in Supplementary Section 3.2. We extracted the maximum pump-induced rotation angle from the extremum of this function, which occurs at $t_{max} = \sigma_2 \ln\left(\frac{\tau_2+\sigma_2}{\sigma_2}\right)$. The values of $\theta(t_{max})$ as a function of temperature, pump electric field and pump wavelength (and the corresponding induced magnetic moments; see below) are plotted in Fig. 5. The vertical error bars were derived from the 1σ confidence interval of the fit. The horizontal error bars in Fig. 5b, c denote the systematic uncertainty of the THz power calibration and the FWHM of the pump spectrum, respectively.

Experimental determination of induced magnetic moment. The magnetic moment induced by the THz pump was determined from the measured pump-induced Faraday rotation angle. The Faraday effect relates the rotation angle θ of linearly polarized light passing through a medium of thickness L to a magnetic flux density B via the relation $\theta = VBL$, where V is the Verdet constant. In the absence of an external magnetic field, this becomes $\theta = \mu_0 VML$, where M is the magnetization of the medium and μ_0 is the vacuum magnetic permeability.

In our experiment, we induced a magnetization that varied as a function of depth because of the finite penetration depth δ of the pump pulse. The probe penetration depth was much larger than the sample thickness[38,39] (approximately 1 mm at 880 nm), so the measured rotation angle arises from an integration of the induced magnetization over the entire sample: $\theta = \mu_0 V \int_0^L M(x)dx$. The pump intensity decays exponentially within the material (over the length scale δ), and, as shown in Fig. 5b in the main text, the induced M scales linearly with the pump intensity. Then, the induced magnetization at the surface of the material becomes $M_{ind} = \frac{\theta}{\mu_0 V\delta(1-e^{-L/\delta})}$.

Using the Verdet constant determined from static magnetic field measurements[24] $V = 2.4° \, cm^{-1} \, G^{-1}$, we find $M_{ind} = (28 \pm 3)$ G for the maximum rotation angle of 0.44 ± 0.02 mrad induced by the pump at 12 THz ($\delta = 3.8$ μm). Taking the volume of the CoF_2 unit cell (70.099 Å^3, as measured by X-ray diffraction[4]), this induced magnetization corresponds to an induced moment of $m_{ind} = (0.21 \pm 0.03)$ μ_B per unit cell. The values of m_{ind} in Fig. 5b, c were computed in the same manner as above for all pump intensities and wavelengths. The value and uncertainty of the maximum rotation angle were extracted from fits to the time-dependent Faraday rotation data, as described above. The penetration depth was determined from the measured optical conductivity (shown in Fig. 3a in the main text).

Theoretical modelling. As discussed in the main text, first-principles calculations in the framework of density functional theory were performed to gain understanding of the microscopic mechanism and to estimate the magnitude of the optically induced ferrimagnetic moment. The computational details and results—including the equilibrium structural parameters, effect of optical driving, and comparison to static strain—are provided in Supplementary Section 2.

The phenomenological model developed to describe the magnetization dynamics (Fig. 6) is detailed in Supplementary Section 3.

Data availability

Source data are available for Figs. 4–6. All other data that support the plots within this paper and other findings of this study are available from the corresponding author on reasonable request.

References

37. Baruchel, J., Schlenker, M. & Barbara, B. 180° antiferromagnetic domains in MnF_2 by neutron topography. *J. Magn. Magn. Mater.* **15–18**, 1510–1512 (1980).
38. Van Der Ziel, J. P. & Guggenheim, H. J. Optical spectrum of CoF_2. *Phys. Rev.* **166**, 479–487 (1968).
39. Zimring, L. J. & Stout, J. W. Polarized crystal spectra of CoF_2 and $Co_{0.06}Zn_{0.94}F_2$. *J. Chem. Phys.* **51**, 4197–4209 (1969).

Acknowledgements

We thank J. Chen for help preparing the samples and assistance with the optical experiment. This work received funding from the European Research Council under the European Union's Seventh Framework Programme (FP7/2007–2013)/ERC (grant agreement no. 319286 (QMAC)) and the Cluster of Excellence 'CUI: Advanced Imaging of Matter' of the Deutsche Forschungsgemeinschaft (DFG), EXC 2056, project ID 390715994. Work done at the University of Oxford was funded by EPSRC grant no. EP/M020517/1, entitled Oxford Quantum Materials Platform Grant. A.S.D. was supported by a fellowship from the Alexander von Humboldt Foundation.

Author contributions

P.G.R. and A.C. planned the project together with A.S.D. and M. Först. A.S.D. designed and performed the experiments with help from B.L., T.F.N. and M. Först. A.S.D. analysed the experimental data. M. Fechner carried out the first-principles calculations. M. Fechner, A.S.D. and P.G.R. developed the phenomenological model. D.P. prepared the samples. A.S.D. and A.C. wrote the manuscript with feedback from all co-authors.

Competing interests

The authors declare no competing interests.

Additional information

Supplementary information is available for this paper at https://doi.org/10.1038/s41567-020-0936-3.

Correspondence and requests for materials should be addressed to A.S.D. or A.C.

Reprints and permissions information is available at www.nature.com/reprints.